High-Quality-Factor AlGaAs-On-Sapphire Microring Resonators

Zheng, Yi; Pu, Minhao; Sahoo, Hitesh Kumar; Semenova, Elizaveta; Yvind, Kresten

Published in:
Journal of Lightwave Technology

Link to article, DOI:
10.1109/JLT.2018.2882305

Publication date:
2018

Document Version
Peer reviewed version

High-Quality-Factor AlGaAs-On-Sapphire Microring Resonators

Yi Zheng, Minhao Pu, Hitesh Kumar Sahoo, Elizaveta Semenova, and Kresten Yvind

***Abstract*—We realize an AlGaAs-on-sapphire platform through Al_2O_3-assisted direct wafer bonding and substrate removal processes. The direct wafer bonding process is optimized concerning the intermediate layer deposition and annealing temperature to obtain a high bonding strength between the AlGaAs and sapphire wafers. High quality-factor (Q) microring resonators are fabricated using electron-beam lithography in which the charging effect is mitigated by applying a thin aluminum layer, and a smooth pattern sidewall definition is obtained using a multi-pass (exposure) process. We achieve an intrinsic Q of up to ~460,000, which is the highest Q for AlGaAs microring resonators. Taking advantage of such high Q resonators, we demonstrate an ultra-efficient nonlinear four-wave mixing process in this platform and obtain a conversion efficiency of -19.8 dB with continuous-wave pumping at a power level of 380 μW. We also investigate the thermal resonance shift of microring resonators with different substrate layouts and observe superior temperature stability for devices in the AlGaAs-on-sapphire platform. The realization of the AlGaAs-on-sapphire platform also opens new prospects for AlGaAs devices in nonlinear applications in the mid-infrared wavelength range.**

***Index Terms*—Integrated optics, optics resonators, nonlinear optics, four-wave mixing.**

I. Introduction

ALUMINUM gallium arsenide ($Al_xGa_{1-x}As$) is a promising candidate for integrated nonlinear photonics due to its high material nonlinearity and wide transparency wavelength range [1], [2]. High quality-factor (Q) microring resonators are essential components for enhancing the efficiency of nonlinear processes such as second-harmonic generation [3], four-wave mixing (FWM) [4], stimulated Raman scattering [5] and stimulated Brillouin scattering [6]. Since GaAs/AlGaAs microring resonators were first reported to improve FWM conversion efficiency [7], significant efforts have been made to realize low loss AlGaAs components [8], [9]. However, the performance of the demonstrated AlGaAs devices were limited due to relatively weak light confinement and challenging etching processes for conventional high aspect ratio AlGaAs waveguides [9]–[12]. To enhance the device nonlinearity and relax the deep etching requirement, a high-index-contrast AlGaAs-on-insulator (AlGaAsOI) waveguide platform was proposed and realized using recently developed fabrication processes [13], [14]. The high index contrast was accomplished by embedding a thin (250-400 nm) patterned layer of $Al_xGa_{1-x}As$ in a low-index material, SiO_2. Ultra-high effective nonlinearity was demonstrated for low-loss nano-waveguides in this platform. Since the bandgap of the $Al_xGa_{1-x}As$ can be engineered by changing the aluminum composition (x) to avoid the nonlinear loss induced by the two-photon absorption in the telecom wavelength range, a variety of nonlinear applications such as frequency comb generation [14], [15], parametric wavelength conversion [16], [17], and supercontinuum generation [18] have been demonstrated in the AlGaAsOI platform. However, the low index oxide layer between the $Al_xGa_{1-x}As$ and the carrier substrate has strong material absorption at wavelengths longer than 2.5 μm [19], which prohibits extending the operation wavelength range for the nonlinear AlGaAsOI platform into the mid-infrared (MIR) range. The MIR wavelength region (2-20 μm) is of great interest for various spectroscopy applications [20] as the characteristic rovibrational transition of most light molecules lie in this spectral range. Sapphire can be used as a substrate material to extend the operation wavelength range of AlGaAs devices to 6 μm, in a similar way as it has been used in the silicon-on-sapphire platform [21]–[23] where a thin silicon layer was epitaxially grown on a sapphire substrate. However, a high-quality AlGaAs layer cannot be grown on a sapphire substrate due to the lattice mismatch. Therefore, a wafer bonding process is required to realize an AlGaAs-on-sapphire (AlGaAsOS) wafer. Besides, sapphire offers a high thermal conductivity (25-50 $Wm^{-1}K^{-1}$, depending on its crystal plane), which is an order of magnitude larger than that of silica. Therefore, compared with AlGaAsOI devices, AlGaAsOS devices are expected to offer improved temperature stability. In this paper, we realize AlGaAsOS wafers using an Al_2O_3-assisted direct wafer bonding (DWB) process [24]. We optimize the device patterning process especially for this platform and achieve a high Q of nearly half a million for a microring resonator in which we demonstrate a highly-efficient FWM process. Moreover, we present an $\sim$ 80% reduction of thermally-induced resonance shift for AlGaAsOS resonators compared with the AlGaAsOI devices.

II. Fabrication

An $Al_xGa_{1-x}As$ layer and a dual-etch stop layer consisting of two InGaP layers with a GaAs layer in between were epitaxially grown on a GaAs substrate in a low-pressure metal-organic vapor-phase epitaxial (MOVPE) reactor [13]. An aluminum composition (x) of 12% was used for the experimental data below. The $Al_xGa_{1-x}As$ and sapphire (c-plane)

Manuscript received April 19, 2005; revised September 17, 2014.; accepted November 24, 2017. Date of publication November 29, 2017; date of current version January 8, 2018. (Corresponding author: Minhao Pu.)

The authers are with the Department of Photonics Engineering, Technology University of Denmark, Building 343, DK-2800 Kgs.Lyngby, Denmark.(email: yizhen@fotonik.dtu.dk, mipu@fotonik.dtu.dk, hikus@fotonik.dtu.dk, esem@fotonik.dtu.dk, kryv@fotonik.dtu.dk)

This article has been accepted for publication in a future issue of this journal, but has not been fully edited. Content may change prior to final publication. Citation information: DOI 10.1109/JLT.2018.2882305, Journal of Lightwave Technology

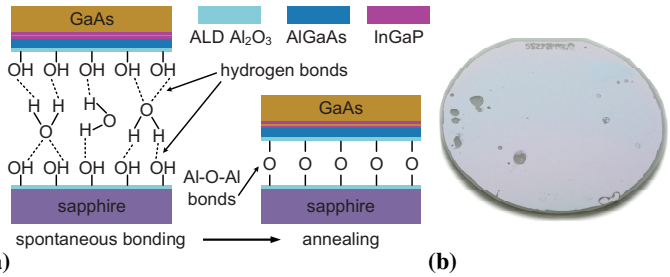

Fig. 1. (a) Schematic illustration of the Al_2O_3-assisted direct wafer bonding (DWB) process: spontaneous bonding and annealing. (b) Photo for a bonded 2-inch wafer after the substrate removal processes.

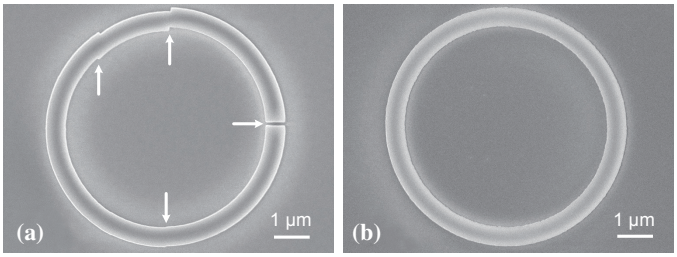

Fig. 2. Scaning electron microscopy (SEM) pictures of ring patterns in developed HSQ without (a) and with (b) applying a 20-nm thick aluminum layer in electron-beam lithography (EBL).

wafers were bonded by a DWB process. Wafer cleanliness and surface roughness are two critical elements for DWB as small particles or rough surfaces result in delamination of bonded wafers. Therefore, RCA cleaning and careful wafer handling are necessary for a successful DWB. The measured root mean square (RMS) surface roughness for the $Al_xGa_{1-x}As$ and sapphire wafers are 0.21 nm and 0.15 nm, respectively, which are small enough (<0.5 nm) for the DWB process [25].

High-quality wafer bonding also depends on the density of -OH groups at the bonding surfaces, especially for spontaneous bonding processes at room temperature. A commonly used intermediate layer material SiO_2 typically has a density of -OH groups of 4 OH/nm^2 at its surface [26] while a much higher density (18 OH/nm^2) can be expected for Al_2O_3 surfaces [27]. Therefore, Al_2O_3 was used as the intermediate layer material for our DWB process. We deposited a 3-nm thick Al_2O_3 layer on both AlGaAs and sapphire wafers using atomic layer deposition (ALD) at 250°C. The deposition temperature was optimized to avoid Al-O-Al bond formation that consumes -OH groups at the deposition surfaces. A high density of -OH groups can be formed at Al_2O_3 surfaces, which makes the surfaces highly hydrophilic enabling easy spontaneous bonding based on van der Waals forces and hydrogen bonds [28] as shown in Fig. 1(a). The spontaneous bonding was done immediately after ALD to avoid any loss of the generated -OH groups.

The bonded wafer was annealed with a 4-kN force applied for 30 minutes to increase the bonding strength by creating strong Al-O-Al bonds as shown in Fig. 1(a). The annealing temperature and the intermediate Al_2O_3 layer thickness are critical parameters for the DWB process. High-temperature annealing is commonly used to increase the density of Al-O-Al bonds. However, more H_2O will be formed at the bonding interface, which may result in micro voids if there is no out-gassing channel for H_2O [29]. For instance, micro void generation was observed after annealing at 450°C. A too high annealing temperature may also lead to wafer bowing or cracking because of the large thermal expansion coefficient difference (23%) between $Al_xGa_{1-x}As$ and sapphire (c-plane) materials. Void-free bonding can be achieved with annealing at 300°C. The H_2O generated during the Al-O-Al bond formation can be consumed in a finite oxidation process at the $Al_xGa_{1-x}As$ surface, which also consumes a few nanometers of $Al_xGa_{1-x}As$ [30]. It is also essential to use a very thin intermediate layer since a too thick (e.g., 35 nm) intermediate Al_2O_3 layer may prohibit such an oxidation process and induce micro voids during the annealing process since the generated H_2O cannot escape from the bonding interface [29].

We measured the bonding strength of the bonded wafer by using the razor blade crack length test [31] and obtained a bonding strength of 1000 mJ/m^2, which is much higher than that of a similar Al_2O_3-assisted DWB for an $InGaAsP - SiO_2$ bonding interface (600 mJ/m^2) [32]. Such a low-temperature Al_2O_3-assisted DWB process can also be applied to larger wafers. Our bonding tests for 4-inch silicon wafers also show a high bonding yield.

The last process step to fabricate an AlGaAsOS wafer is substrate removal with chemical etching [13]. It is worth noting that a dual-etch stop layer is essential to obtain a smooth AlGaAs surface during the chemical etching process. To get uniform chemical etching, we removed the unwanted thin Al_2O_3 film deposited on the backside of the $Al_xGa_{1-x}As$ wafer during the ALD process through chlorine-based dry etching. Figure 1(b) shows a fabricated AlGaAsOS wafer which is ready for device fabrication.

The device fabrication on the AlGaAsOS wafer starts with pattern definition by electron beam lithography (EBL) in hydrogen silsesquioxane (HSQ), a high resolution resist that was spun on an AlGaAsOS wafer where a 300-nm thick $Al_xGa_{1-x}As$ layer resides on a 430-μm thick sapphire substrate. EBL was performed using a JEOL system (JBX-9500FS) at 100-keV. Compared with the AlGaAsOI wafer where the insulating SiO_2 layer is only 3-μm thick and sandwiched by semiconductor materials, the AlGaAsOS wafer suffers more from charging effects in the standard EBL process [33] as the whole substrate is insulating and the projected electrons cannot be dissipated efficiently. In the standard EBL process, device patterns are pre-fractured by a pattern generator software into segments and then defined in HSQ by electron-beam exposing different segments one by one. The accumulated charges in the exposed segments will deflect the electron beam when exposing the adjacent segments, which results in pattern dislocation as observed for a microring pattern defined in HSQ as shown in Fig. 2(a) (denoted by arrows). A multi-pass (exposure) process has been reported to be an efficient method to reduce charging-induced segment stitching errors in the AlGaAsOI platform [13]. However, applying the multi-pass process in the AlGaAsOS platform results in an even worse pattern definition than Fig. 2(a) due to a large

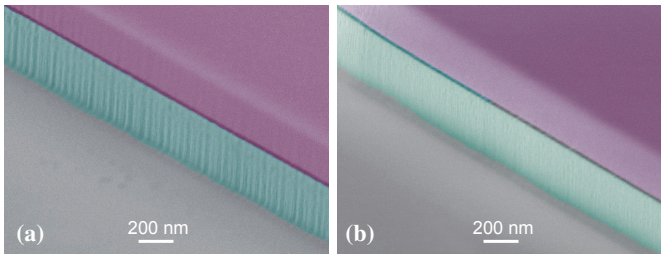

Fig. 3. SEM pictures of etched patterns that defined in EBL with a standard single-pass process (a) and a multi-pass process (b). The AlGaAs layer is highlighted in blue and the HSQ layer in purple.

misalignment between consecutive passes (exposures). The misalignment indicates that excessive charge was accumulated in the sapphire layer and difficult to dissipate.

To mitigate the charging effect, a 20-nm thick aluminum layer was deposited on top of the electron-beam resist (HSQ) layer by thermal evaporation before the EBL process. As a light metal, aluminum is almost transparent to a high-voltage electron beam, but it can be used as an effective screen of electric fields, shielding the exposing electron beam from the charges accumulated in the sapphire substrate during an EBL process [34]. In this way, a microring pattern can be well defined without any discontinuity as shown in Fig. 2(b).

The HSQ pattern was then transferred to the $Al_xGa_{1-x}As$ layer using a boron trichloride (BCl_3)-based dry etching process in an inductively coupled plasma reactive ion etching (ICP-RIE) machine [13]. Although the aluminum layer was used during the standard EBL process, stripe-like roughness was observed at pattern sidewalls as shown in Fig. 3(a). This is due to the imperfect electron-beam shot arrangement from the pre-fracturing and the deflection noise during the EBL process. The electron-beam shot arrangement at the edge region between the pre-fractured segments is normally not as uniform as at other patterning regions which may result in small stitching imperfections at the pattern boundary. Therefore, an averaging technique such as the multi-pass (exposure) process [13] is highly desired. Only after using the multi-pass exposure technique with the aluminum layer could a significant improvement concerning the sidewall roughness be obtained, as shown in Fig. 3(b). All the process settings and parameters are described in [13].

III. Linear Characterization

In the EBL process, the different fracturing for straight and curved patterns results in different waveguide loss performance according to the electron-beam shot arrangements at the waveguide edges. To investigate the influence of the multi-pass process on patterning straight and curved waveguides, we characterized microring and racetrack resonators as shown in Fig. 4(a). Figure 4(b) and 4(c) show SEM pictures of a fabricated 17-μm radius microring resonator and its coupling region with a 300 nm bus-to-ring gap, respectively. The waveguide widths for the resonator and the bus are 610 nm and 440 nm, respectively. The devices were cladded with silica to avoid any particle contamination because ambient particles may deposit on the waveguide surfaces and become scattering

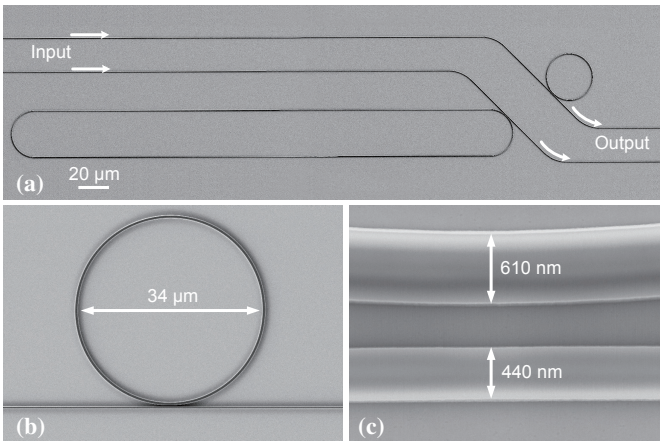

Fig. 4. SEM pictures of fabricated microring and racetrack resonators (a), a 17-μm radius microring resonator (b) and its coupling region (c).

sources or local heating sources (under high power operation), which results in degradation of device performance. It should be noted that the silica cladding should be avoided to ensure a fully accessible transparency window of AlGaAs-on-sapphire platform, especially for nonlinear applications in the MIR region. Finally, the sample was cleaved to form the input and output facets, where bus waveguides are tapered to large dimension to facilitate chip-to-fiber coupling for characterization. Microring resonators with different bus-to-ring coupling gaps have been characterized to determine the correlation between the coupling condition and coupling gaps. Figure 5 shows the normalized transmission spectra of 17-μm radius microring resonators (Fig. 5(a,b,c)) and 810-μm long racetrack resonators (Fig. 5(d,e,f)), which all operated in under-coupled conditions. The free spectral ranges (FSRs) of the microring and racetrack resonators are 727 GHz and 99 GHz, respectively, as shown in Fig. 5(a,d) where only one mode family is observed for both resonators. We fabricated the aforementioned microresonators using different EBL processes (the standard single-pass process for Fig. 5(b,e) and the multi-pass process for Fig. 5(c,f)). The solid lines show Lorentzian fitting of those resonances. The intrinsic quality factor (Q_{int}) is calculated using the equation $Q_{int} = 2Q_{load}/(1+\sqrt{T_0})$ for under-coupled devices [35], where Q_{load} is the measured loaded quality factor and T_0 is the fraction of transmitted optical power at the resonance wavelength. To extract Q_{int}, we characterized five devices for each fabrication condition. The estimated intrinsic Qs for microring resonators fabricated with the single-pass and multi-pass EBL processes are $(1.3 \pm 0.28) \times 10^5$ and $(2.4 \pm 0.25) \times 10^5$, respectively, which indicates that the linear loss of a curved waveguide was improved significantly from 4.8 dB/cm to 2.7 dB/cm. The multi-pass process ensured a much smoother definition of curved waveguides. The fabricated racetrack resonators consist of 17-μm radius curved waveguide and 700-μm long straight waveguide parts. Their intrinsic Qs are highly dependent on the linear loss of the straight waveguides. Figure 5(c) and 5(f) show that the multi-pass process also leads to an improvement of Q by approximately a factor of two. The estimated intrinsic Qs for the racetrack resonators fabricated with single-

This article has been accepted for publication in a future issue of this journal, but has not been fully edited. Content may change prior to final publication. Citation information: DOI 10.1109/JLT.2018.2882305, Journal of Lightwave Technology

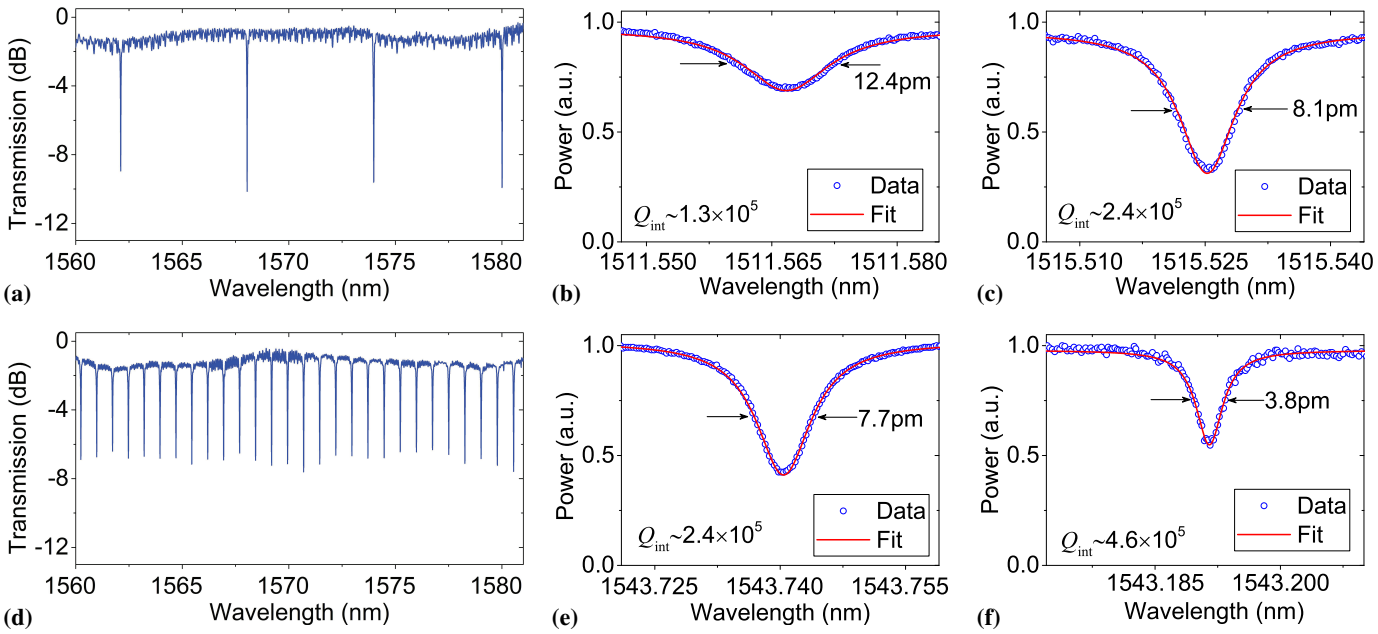

Fig. 5. Measured (normalized) transmission spectra for 17-μm radius microring resonators (a,b,c) and 810-μm long racetrack resonators (d,e,f). Resonators are fabricated using EBL with the standard single-pass process (b, e) and the multi-pass process (c,f).

pass and multi-pass EBL process are $(2.4 \pm 0.25) \times 10^5$ and $(4.6 \pm 0.21) \times 10^5$, respectively, which indicates that the linear loss of the straight waveguide was improved from 2.4 dB/cm to 1.2 dB/cm by using the multi-pass process. Therefore, using the multi-pass process is an effective way to improve performance for both straight and curved waveguides for the AlGaAsOS platform when an electrical-field shield layer is applied. As shown in Fig. 5(f), we achieved an intrinsic Q of 4.6×10^5 for a 99-GHz-FSR device, which is the highest reported Q for AlGaAs microring resonators.

IV. Nonlinear Characterization

Benefitting from the high Qs, ultra-efficient nonlinear processes can be expected in AlGaAsOS microring resonators. We performed FWM experiments in the setup shown in Fig. 6(a). Continuous-wave (CW) signal and pump waves were generated through tunable external-cavity lasers (ECLs) and combined using a 3-dB coupler. The pump wave was amplified by an erbium-doped fiber amplifier (EDFA) to compensate the fiber-to-chip coupling losses (10 dB/facet) and subsequently filtered by a 1-nm optical band-pass filter (BPF). Both signal and pump waves were aligned with polarization controllers (PCs) to the TE polarization of the AlGaAsOS waveguide. Tapered fibers were used to couple light into and out of the chip, and the output spectrum was recorded by an optical spectrum analyzer (OSA). The 810-μm long racetrack resonator under test operated in slightly under-coulped condition with a loaded Q of around 213,000 (the resonance linewidth is shown in Fig. 6(b)). Figure 6(c) shows the output spectra from the resonator when the pump and signal waves are both off-resonance (grey line) and on-resonance with (red line) and without (green curve) the signal wave. We achieved an overall conversion efficiency (CE), defined by the ratio between the output idler power and input signal power in the bus waveguide of -19.8 dB with only 380 μW of pump power. Figure 6(d) shows the measured CE as a function of coupled pump power in the bus waveguide. Compared with the result reported for conventional AlGaAs microring resonators [12], the achieved maximum CE is more than two orders of magnitude higher at a pump power level which is more than one order of magnitude lower. This ultra-high efficient nonlinear process is enabled by a combination of strong light confinement from the high-index-contrast waveguide layout and well-developed device fabrication processes.

V. Thermal Characterization

In high Q resonators, a small perturbation of the input power may result in a relatively large intracavity power change and thus a significant resonance shift, especially for devices made using a material with a large thermo-optic coefficient (TOC) such as AlGaAs ($2.4 \times 10^{-4}\mathrm{K}^{-1}$) [36]. As temperature stable resonators are highly desirable for nonlinear applications such as Kerr comb generation, we investigate how the thermal properties of AlGaAs devices are influenced by their substrates. We compare the thermally-induced resonance shifts in 17-μm radius microring resonators in AlGaAsOI and AlGaAsOS platforms. The chosen AlGaAsOI and AlGaAsOS devices have the identical design in regards to the waveguide cross-sectional dimension (610 nm×300 nm) and the coupling gap (225 nm).

Figure 7(a) and Fig. 7(b) show the measured normalized transmission with different input power for the microring resonators made using AlGaAsOI and AlGaAsOS platforms, respectively. Triangular optical resonance profiles are observed due to power-induced thermal shift during the measurement when scanning the laser from short to long wavelengths. With an injected power of about 4 mW, the resonance shift is around 0.94 nm for the AlGaAsOI device but only 0.22 nm for the AlGaAsOS device. Both samples are fabricated with

This article has been accepted for publication in a future issue of this journal, but has not been fully edited. Content may change prior to final publication. Citation information: DOI 10.1109/JLT.2018.2882305, Journal of Lightwave Technology

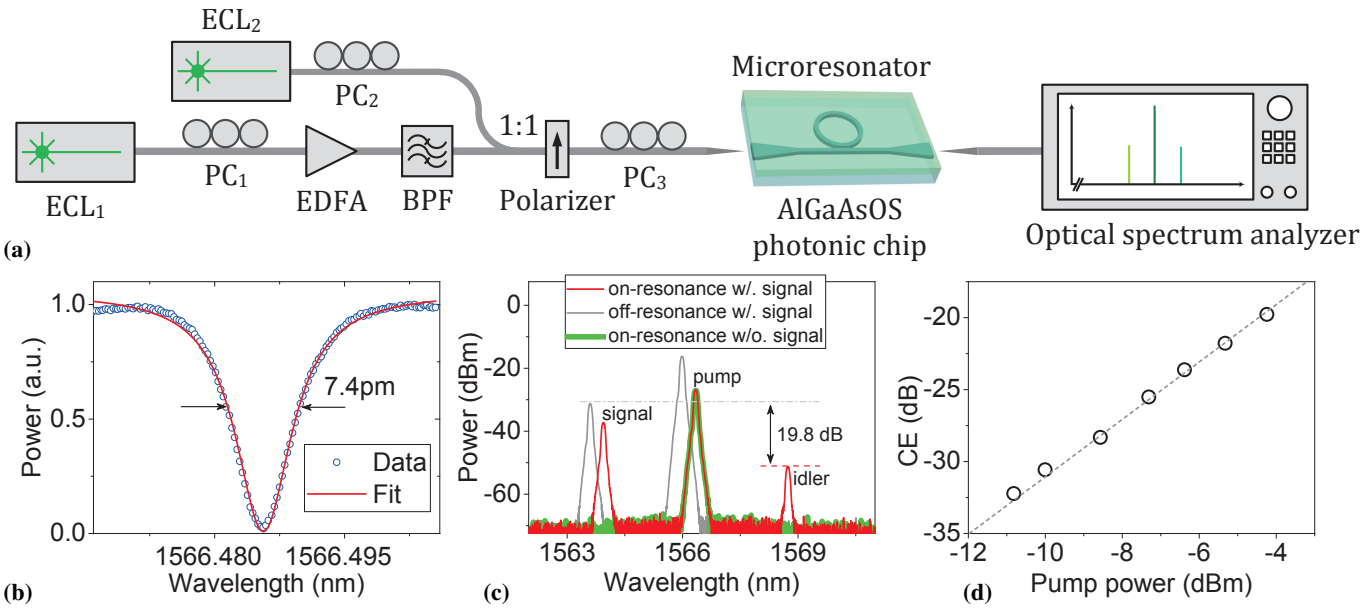

Fig. 6. (a) Schematic of the four-wave mixing (FWM) characterization setup. (b) Measured normalized transmission spectrum of an AlGaAsOS microresonator at 1566 nm. (c) Measured output spectra of the microresonator with the pump and signal waves off-resonance (gray curves) and on-resonance (red curve). The green curve shows the output spectrum when only the pump wave was coupled into the microresonator. (d) Measured FWM conversion efficiency (CE) for the microresonator as a function of the pump power in the bus waveguide.

the same parameter settings for all the processes from crystal growth to dry-etching to ensure the same surface properties (e.g. absorption and scattering). Therefore, the reduced thermally-induced resonance shift for the AlGaAsOS device is mainly attributed to the high thermal conductivity of the sapphire substrate given that the intracavity power is the same for both devices. We measured the thermally-induced resonance shift of three microring resonators for each platform. All those resonators have the same aforementioned design parameters, similar intrinsic Qs (~220,000) and similar coupling conditions.

Figure 7(c) shows the power buildup factor as a function of the coupling coefficient, and the data points correspond to the devices used in the comparison. The power buildup factor is defined as the ratio between intracavity power and power in the bus waveguide. At the resonance wavelength, the power buildup factor can be estimated by $\kappa^2/(1-a\tau)^2$ [7], where a, κ and τ are the round trip amplitude transmission, the coupling coefficient and the transmission coefficient, respectively. Here κ^2 and τ^2 are the power splitting ratios of the bus-to-ring coupler. They are assumed to satisfy $\kappa^2 + \tau^2 = 1$ and can be calculated using the equation $T_0 = (a-\tau)^2/(1-a\tau)^2$ [37] provided that the transmission at the resonance wavelength T_0 is extracted from a measurement. Our AlGaAsOI sample has a slightly higher aluminum composition (17%) than our AlGaAsOS sample. We performed the thermal resonance shift experiment at a relatively low power level to avoid any nonlinear absorption-induced thermal effect. As shown in Fig. 7(d), the measured resonance shift scales linearly with the coupled power. The linear fitting of the measured data shows an 80% reduction of thermally-induced resonance shift for devices with a sapphire substrate, indicating that the sapphire substrate is very efficient for thermal dissipation. Since an improved thermal conductivity for microresonators is critical for accessing soliton states (especially the single soliton state) for Kerr comb generation [38], the demonstrated AlGaAsOS platform is promising in comb applications. Further improvement of temperature stability for this platform could be achieved by replacing the top cladding material SiO_2 with a high thermal conductivity material such as Al_2O_3 or a material with negative TOC such as TiO_2.

VI. Conclusion

In conclusion, we have realized a new integrated AlGaAsOS platform using direct wafer bonding and substrate removal processes. The patterning fabrication process has been optimized for this platform, where we have obtained an intrinsic Q of 4.6×10^5 for a 810-μm long racetrack resonator. We have also achieved a FWM conversion efficiency of -19.8 dB with only 380 μW CW pump power. Thanks to the high thermal conductivity of sapphire, a significant improvement of temperature stability has been obtained for the AlGaAsOS microring resonators compared with the AlGaAsOI counterparts, which is potentially beneficial to applications such as frequency comb generation [38], wavelength division multiplexing [39], and high speed modulation [40]. Moreover, the realization of the AlGaAsOS platform also opens new possibilities for nonlinear $\chi^{(2)}$ and $\chi^{(3)}$ AlGaAs devices for MIR applications.

VII. Acknowledgment

The authors would like to acknowledge financial support from DNRF Research Centre of Excellence, SPOC (DNRF123) and Villum Foundation's Centre of Excellence, NATEC II. The authors also thank Peter Girouard at Technical University of Denmark for his helpful comments on this letter.

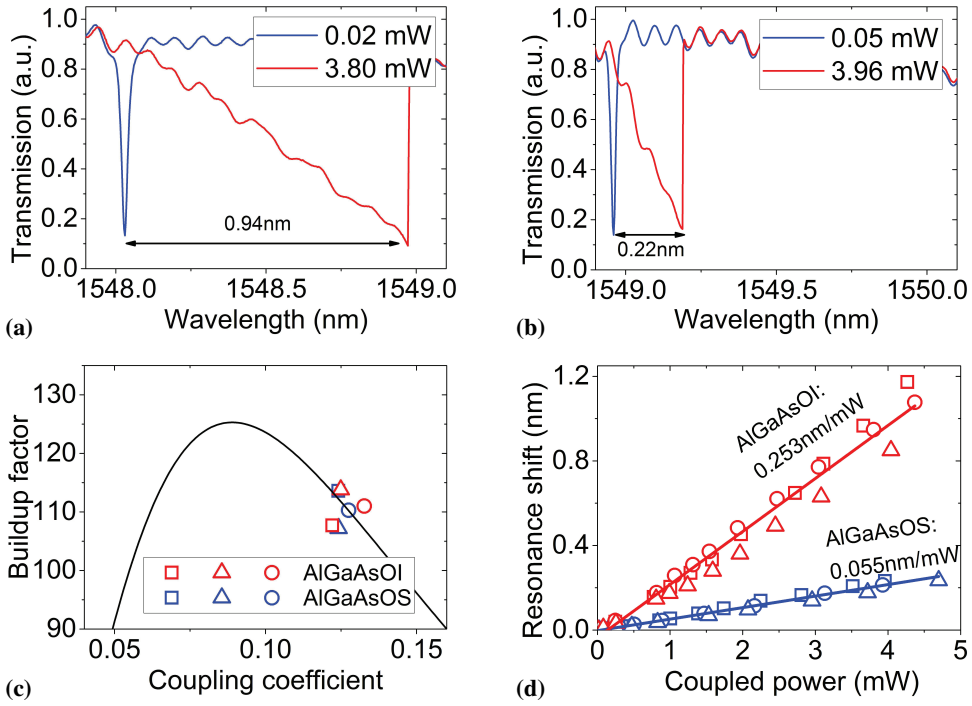

Fig. 7. Measured (normalized) transmission spectra showing resonance shift at different input power levels for 17-μm radius microring resonators with similar Q but made in different platoforms (AlGaAsOI (a) and AlGaAsOS (b)). (c) Estimated build-up factors of the microring resonators used in the test. (d) Measured resonance shifts as a function of coupled power in the bus waveguides. Data points in (c) and (d) are extracted from the characterization of three microring resonators with similar Qs and coupling conditions for each platform. .

REFERENCES

[1] G. Stegeman, A. Villeneuve, J. Kang, J. Aitchison, C. Ironside, K. Al-Hemyari, C. Yang, C.-H. Lin, H.-H. Lin, G. Kennedy, and W. Sibbett, "AlGaAs below half bandgap: the silicon of nonlinear optical materials," *J. Nonlinear Opt. Phys. Mater.*, vol. 3, no. 03, pp. 347–371, 1994.

[2] J. S. Aitchison, D. Hutchings, J. Kang, G. Stegeman, and A. Villeneuve, "The nonlinear optical properties of AlGaAs at the half band gap," *IEEE J. Quanum Electron.*, vol. 33, no. 3, pp. 341–348, 1997.

[3] Z. Yang, P. Chak, A. D. Bristow, H. M. van Driel, R. Iyer, J. S. Aitchison, A. L. Smirl, and J. Sipe, "Enhanced second-harmonic generation in AlGaAs microring resonators," *Opt. Lett.*, vol. 32, no. 7, pp. 826–828, 2007.

[4] M. Ferrera, L. Razzari, D. Duchesne, R. Morandotti, Z. Yang, M. Liscidini, J. Sipe, S. Chu, B. Little, and D. Moss, "Low-power continuous-wave nonlinear optics in doped silica glass integrated waveguide structures," *Nature Photon.*, vol. 2, no. 12, pp. 737–740, 2008.

[5] S. Spillane, T. Kippenberg, and K. Vahala, "Ultralow-threshold raman laser using a spherical dielectric microcavity," *Nature*, vol. 415, no. 6872, pp. 621–623, 2002.

[6] B. J. Eggleton, C. G. Poulton, and R. Pant, "Inducing and harnessing stimulated brillouin scattering in photonic integrated circuits," *Advan. Opt. and Photon.*, vol. 5, no. 4, pp. 536–587, 2013.

[7] P. P. Absil, J. V. Hryniewicz, B. E. Little, P. S. Cho, R. A. Wilson, L. G. Joneckis, and P.-T. Ho, "Wavelength conversion in GaAs micro-ring resonators," *Opt. Lett.*, vol. 25, no. 8, p. 554, 2000.

[8] M. Volatier, D. Duchesne, R. Morandotti, R. Ares, and V. Aimez, "Extremely high aspect ratio GaAs and GaAs/AlGaAs nanowaveguides fabricated using chlorine ICP etching with N_2-promoted passivation," *Nanotechnol.*, vol. 21, no. 13, p. 134014, 2010.

[9] J. J. Wathen, P. Apiratikul, C. J. Richardson, G. A. Porkolab, G. M. Carter, and T. E. Murphy, "Efficient continuous-wave four-wave mixing in bandgap-engineered AlGaAs waveguides," *Opt. Lett.*, vol. 39, no. 11, pp. 3161–3164, 2014.

[10] K. Dolgaleva, W. C. Ng, L. Qian, and J. S. Aitchison, "Compact highly-nonlinear AlGaAs waveguides for efficient wavelength conversion," *Opt. Express*, vol. 19, no. 13, pp. 12 440–12 455, 2011.

[11] C. Lacava, V. Pusino, P. Minzioni, M. Sorel, and I. Cristiani, "Nonlinear properties of AlGaAs waveguides in continuous wave operation regime," *Opt. Express*, vol. 22, no. 5, pp. 5291–5298, 2014.

[12] P. Kultavewuti, V. Pusino, M. Sorel, and J. S. Aitchison, "Low-power continuous-wave four-wave mixing wavelength conversion in AlGaAs-nanowaveguide microresonators," *Opt. Lett.*, vol. 40, no. 13, pp. 3029–3032, 2015.

[13] L. Ottaviano, M. Pu, E. Semenova, and K. Yvind, "Low-loss high-confinement waveguides and microring resonators in AlGaAs-on-insulator," *Opt. Lett.*, vol. 41, no. 17, pp. 3996–3999, 2016.

[14] M. Pu, L. Ottaviano, E. Semenova, and K. Yvind, "Efficient frequency comb generation in AlGaAs-on-insulator," *Optica*, vol. 3, no. 8, pp. 823–826, 2016.

[15] H. Hu, F. Da Ros, M. Pu, F. Ye, K. Ingerslev, E. P. da Silva, M. Nooruzzaman, Y. Amma, Y. Sasaki, T. Mizuno, Y. Miyamoto, L. Ottaviano, E. Semenova, P. Guan, D. Zibar, M. Galili, K. Yvind, T. Morioka, and L. K. Oxenløwe, "Single-source chip-based frequency comb enabling extreme parallel data transmission," *Nature Photon.*, vol. 12, no. 8, p. 469, 2018.

[16] M. Pu, H. Hu, L. Ottaviano, E. Semenova, D. Vukovic, L. K. Oxenløwe, and K. Yvind, "Ultra-efficient and broadband nonlinear AlGaAs-on-Insulator chip for low-power optical signal processing," *Laser & Photonics Reviews*, https://doi.org/10.1002/lpor.201800111, 2018.

[17] F. Da Ros, M. P. Yankov, E. P. da Silva, M. Pu, L. Ottaviano, H. Hu, E. Semenova, S. Forchhammer, D. Zibar, M. Galili, , K. Yvind, and L. K. Oxenløwe, "Characterization and optimization of a high-efficiency AlGaAs-On-Insulator-based wavelength converter for 64-and 256-QAM signals," *IEEE J. Lightw. Technol.*, vol. 35, no. 17, pp. 3750–3757, 2017.

[18] M. Pu, H. Ji, H. Hu, L. Ottaviano, E. Semenova, P. Guan, L. K. Oxenløwe, and K. Yvind, "Supercontinuum generation in AlGaAs-on-insulator nano-waveguide at telecom wavelengths," in *Conference on Lasers and Electro-Optics (CLEO)*, 2016, p. AM3J.3.

[19] R. Kitamura, L. Pilon, and M. Jonasz, "Optical constants of silica glass from extreme ultraviolet to far infrared at near room temperature," *Appl. Opt.*, vol. 46, no. 33, pp. 8118–8133, 2007.

[20] A. Schliesser, N. Picqué, and T. W. Hänsch, "Mid-infrared frequency combs," *Nature Photon.*, vol. 6, no. 7, pp. 440–449, 2012.

[21] A. Spott, Y. Liu, T. Baehr-Jones, R. Ilic, and M. Hochberg, "Silicon waveguides and ring resonators at 5.5 μ m," *Appl. Phys. Lett.*, vol. 97, no. 21, p. 213501, 2010.

[22] F. Li, S. D. Jackson, C. Grillet, E. Magi, D. Hudson, S. J. Madden, Y. Moghe, C. OBrien, A. Read, S. G. Duvall, P. Atanackovic, B. J. Eggleton, and D. J. Moss, "Low propagation loss silicon-on-sapphire

waveguides for the mid-infrared," *Opt. Express*, vol. 19, no. 16, pp. 15 212–15 220, 2011.

[23] R. Shankar, I. Bulu, and M. Lončar, "Integrated high-quality factor silicon-on-sapphire ring resonators for the mid-infrared," *Appl. Phys. Lett.*, vol. 102, no. 5, p. 051108, 2013.

[24] H. K. Sahoo, L. Ottaviano, Y. Zheng, O. Hansen, and K. Yvind, "Low temperature bonding of heterogeneous materials using Al_2O_3 as an intermediate layer," *J. Vac. Sci. Tech. B*, vol. 36, no. 1, p. 011202, 2018.

[25] J. Fan, P. Anantha, C. Liu, M. Bergkvist, H. Wang, and C. S. Tan, "Thermal characteristics of InP-Al_2O_3/Si low temperature heterogeneous direct bonding for photonic device integration," *ECS J. Solid State Science and Technol.*, vol. 2, no. 9, pp. N169–N174, 2013.

[26] M. Digne, P. Sautet, P. Raybaud, P. Euzen, and H. Toulhoat, "Hydroxyl groups on γ-alumina surfaces: A DFT study," *Journal of Catalysis*, vol. 211, no. 1, pp. 1–5, 2002.

[27] A. A. Tsyganenko and P. P. Mardilovich, "Structure of alumina surfaces," *Journal of the Chemical Society, Faraday Transactions*, vol. 92, no. 23, pp. 4843–4852, 1996.

[28] M. Juppo, A. Rahtu, M. Ritala, and M. Leskelä, "In situ mass spectrometry study on surface reactions in atomic layer deposition of Al_2O_3 thin films from trimethylaluminum and water," *Langmuir*, vol. 16, no. 8, pp. 4034–4039, 2000.

[29] M. Yokoyama, R. Iida, Y. Ikku, S. Kim, H. Takagi, T. Yasuda, H. Yamada, O. Ichikawa, N. Fukuhara, and M. Hata, "Formation of III–V-on-insulator structures on Si by direct wafer bonding," *Semiconductor Science and Technology*, vol. 28, no. 9, p. 094009, 2013.

[30] Y. Luo and D. C. Hall, "Nonselective wet oxidation of AlGaAs heterostructure waveguides through controlled addition of oxygen," *IEEE J. Sel. Top. in Quantum Electron.*, vol. 11, no. 6, pp. 1284–1291, 2005.

[31] W. Maszara, G. Goetz, A. Caviglia, and J. McKitterick, "Bonding of silicon wafers for silicon-on-insulator," *J. Appl. Phys.*, vol. 64, no. 10, pp. 4943–4950, 1988.

[32] Y. Ikku, M. Yokoyama, R. Iida, M. Sugiyama, Y. Nakano, M. Takenaka, and S. Takagi, "ALD Al_2O_3 activated direct wafer bonding for III–V CMOS photonics platform," in *Compound Semiconductor Week (CSW/IPRM), 2011 and 23rd International Conference on Indium Phosphide and Related Materials*, 2011, pp. 1–4.

[33] K. Cummings and M. Kiersh, "Charging effects from electron beam lithography," *J. Vac. Sci. Tech. B*, vol. 7, no. 6, pp. 1536–1539, 1989.

[34] K. Cummings, "A study of deposited charge from electron beam lithography," in *J. Vac. Sci. Tech. B*, vol. 8, no. 6. AVS, 1990, pp. 1786–1788.

[35] M. Borselli, T. J. Johnson, and O. Painter, "Beyond the rayleigh scattering limit in high-Q silicon microdisks: theory and experiment," *Opt. Express*, vol. 13, no. 5, pp. 1515–1530, 2005.

[36] E. A. Camargo, H. M. H. Chong, and R. M. De La Rue, "2D Photonic crystal thermo-optic switch based on AlGaAs/GaAs epitaxial structure," *Opt. Express*, vol. 12, no. 4, p. 588, 2004.

[37] W. Bogaerts, P. De Heyn, T. Van Vaerenbergh, K. De Vos, S. Kumar Selvaraja, T. Claes, P. Dumon, P. Bienstman, D. Van Thourhout, and R. Baets, "Silicon microring resonators," *Laser & Photon. Rev.*, vol. 6, no. 1, pp. 47–73, 2012.

[38] Q. Li, T. C. Briles, D. A. Westly, T. E. Drake, J. R. Stone, B. R. Ilic, S. A. Diddams, S. B. Papp, and K. Srinivasan, "Stably accessing octave-spanning microresonator frequency combs in the soliton regime," *Optica*, vol. 4, no. 2, pp. 193–203, 2017.

[39] K. Padmaraju and K. Bergman, "Resolving the thermal challenges for silicon microring resonator devices," *Nanophoton.*, vol. 3, no. 4-5, pp. 269–281, 2014.

[40] K. Padmaraju, J. Chan, L. Chen, M. Lipson, and K. Bergman, "Thermal stabilization of a microring modulator using feedback control," *Opt. Express*, vol. 20, no. 27, pp. 27 999–28 008, 2012.